energies

MDPI

Article

Numerical and Experimental Study of a Novel Additively Manufactured Metal-Polymer Composite Heat-Exchanger for Liquid Cooling Electronics

Gargi Kailkhura, Raphael Kahat Mandel, Amir Shooshtari * and Michael Ohadi

Advanced Heat Exchangers and Process Intensification (AHXPI) Laboratory, Department of Mechanical Engineering, University of Maryland, College Park, MD 20742, USA; gkailkhu@terpmail.umd.edu (G.K.); raphael.k.mandel@gmail.com (R.K.M.); ohadi@umd.edu (M.O.)
* Correspondence: amir@umd.edu

Abstract: In order to meet increasing power-dissipation requirements of the electronics industry, compact, low-cost, and lightweight heat exchangers (HXs) are desired. With proper design, materials, and manufacture, polymer composite heat exchangers could meet these requirements. This paper presents a novel crossflow air-to-water, low-cost, and lightweight metal-polymer composite HX. This HX, which is entirely additively manufactured, utilizes a novel cross-media approach that provides direct heat exchange between air and liquid sides by using connecting fins. A robust numerical model was developed, which includes the dimensional effects of additive manufacturing. The study consists of a simplified 3D CFD model based on ellipsoidal-shaped staggered tube banks for the laminar range. It then uses an analytical approach to compute entire HX performance. The model is validated experimentally within 8% for thermal performance, 12% for air-side impedance, and 18% for water-side impedance. Finally, HX is compared with a conventional CPU radiator and performs within 10% of the conventional unit for reasonable flow rates and pressure-drop ranges. Moreover, HX also provides added design and cost advantages over the conventional unit, which makes the HX a potential candidate for electronic cooling applications.

Keywords: air-to-water HX; cross-media; additive manufacturing; experiment; 3D CFD modeling; ellipsoidal tube banks

Citation: Kailkhura, G.; Mandel, R.K.; Shooshtari, A.; Ohadi, M. Numerical and Experimental Study of a Novel Additively Manufactured Metal-Polymer Composite Heat-Exchanger for Liquid Cooling Electronics. *Energies* **2022**, *15*, 598. https://doi.org/10.3390/en15020598

Academic Editor: Dmitri Eskin

Received: 30 November 2021
Accepted: 6 January 2022
Published: 14 January 2022

1. Introduction

Due to the fact that compact heat exchangers are an integral part of energy exchange processes, their designs have continuously evolved to meet the growing demands of diverse industries. Compact HXs for gas-to-liquid applications typically consist of metal structures configured with different types of fins such as louver fins, wavy fins, and offset-strip fins [1] on the air side. The purpose is to enhance air-side heat transfer rates, since the air-side heat transfer coefficient is typically very low. However, the liquid heat transfer area of such designs is typically only minimally enhanced, as the liquid heat transfer coefficient is already much higher than that of the air. Moreover, it can be difficult to fabricate complex geometries inside narrow liquid-side channels. Thus, compact, lightweight, low-cost, and low thermal resistance HX units are needed to meet increasing power-dissipation requirements of diverse industrial applications.

Due to lightweight, low-cost, and anti-corrosive properties of polymers, several polymer HX designs have been developed [2–6]. However, the lower thermal conductivity of polymer of about 0.2–0.6 W/(m·K) [7] yields relatively higher conductive resistance through the HX structure. One method to resolve this issue is by increasing the thermal conductivity of polymer HXs to up to 20 times by using metal fillers [4] or carbon nanotubes [8,9] in the polymer media. However, extensive research is still required to determine the effect of metal fillers and polymers on effective thermal conductivity and anisotropic properties of

HXs [10]. Another method to fix this issue is to reduce the polymer's wall thickness using thin-walled polymer HXs [11–14], such as crossflow micro-passage HXs [15]. However, such thin structures are limited by manufacturing constraints. Alternatively, recent studies have presented metal-polymer composite HXs such as hybrid polymer HXs [16] and continuous-wire HXs [17,18]. These hybrid polymer HXs consist of copper and polymer helically wound hybrid tubes capable of increasing effective thermal conductivity from 0.1 W/(m·K) to 1 W/(m·K). However, these HXs are constrained in their tube diameter size. Continuous-wire HXs consist of fine metal wires, with diameters as small as 0.105 to 0.25 mm, woven or knitted through plastic walls. They have been compared to pin-fin arrays, which have been reported to deliver the same performance as conventional louvered fin HXs but at 22% less volume [19]. However, these HXs suffer from wire-curvature issues and lack a robust fabrication procedure.

The current paper meets the above challenges by utilizing a novel, entirely additively manufactured, low-cost, and lightweight metal-polymer composite HX [20–22], with effective thermal conductivity in the range of 130 W/m-K [21]. High thermal conductivity metal wires contribute towards effective thermal conductivity while polymer media contribute to a lightweight and low-cost unit. HX uses an optimized finned area on both air-side and liquid-side surfaces to yield better thermal performance than conventional units for liquid cooling applications of electronics.

The additively manufactured metal-polymer composite HX [23,24] comprises an HX core made of polymer and an array of metal wires, which act as fins for both air-side and liquid-side convective heat transfer, as shown in Figure 1. Metal wires can be arranged in a staggered or inline configuration. The heat exchanger can also include additively manufactured integrated liquid manifolds of polymer. Customized 3D printing processes utilize a polymer and a metal head based on a hybrid and innovative approach [25] designed and developed by a few of the co-authors, as described in [20,26]. The polymer head prints layers of polymer media to build air-side and liquid-side channels using FDM while the metal head prints bare metal wires that continuously lay over the polymer media using EFCAM such that they form a direct heat transfer route between the air-side and liquid-side channels. These wires transfer heat effectively, despite low thermal conductivity of the polymer structure, as shown in Figure 1. This concept is referred to as the cross-media approach, and HXs are referred to as integrated cross-media HXs (iCMHXs). HXs are additively manufactured in-house using a customized proprietary 3D printer. HXs are then post-processed by dip-coating them in polyurethane sealant to ensure leak-proof polymer–metal interfaces [24]. Post-processed HXs are then tested and modeled for heat transfer between hot and cold fluids.

As shown in Figure 1c, for a given wire, heat is first transferred directly by convection between hot water and coated wires (R_w), and then by conduction through coated wires (R_{cond}) until it reaches the air side where heat is transferred by convection with cold air (R_a). In addition to the direct heat transfer route, the novelty of the iCMHX design is further enhanced due to in-built integrated manifolds, double liquid pass flow, small diameter metal wires, and, if desired, thick polymer walls. Small diameter wires result in increased heat transfer area per unit mass, while thick polymer walls can result in higher structural integrity independent of low thermal conductivity of the polymer.

The current study first characterizes experimental results of the iCMHX unit, which can be used as a CPU radiator. The experiments are performed for a specified laminar range that replicates the liquid cooling environment. Since iCMHX is additively manufactured, its printing variabilities are statistically studied to obtain the average printed dimensions of the HX. The numerical study is then carried out by using a simplified 3D CFD model based on average geometric dimensions to obtain heat transfer coefficients of the fluids. Overall HX performance is then analytically modeled using these heat transfer coefficients and compared with experiments.

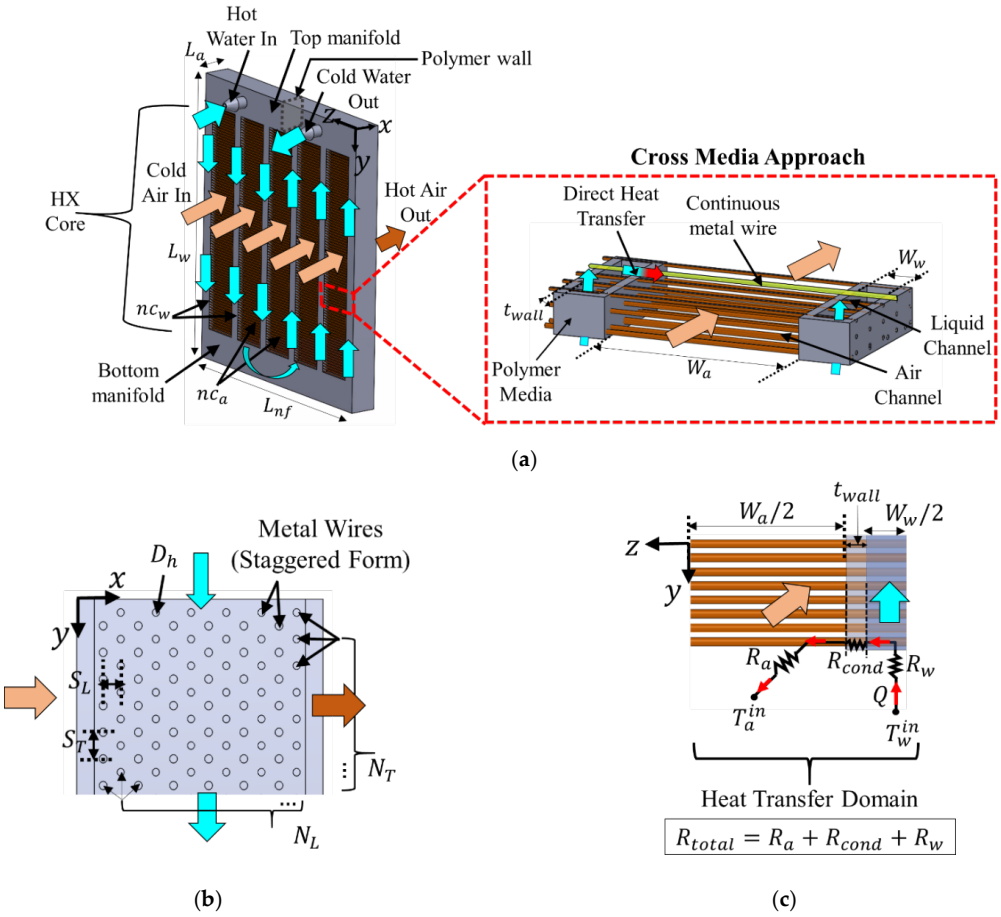

Figure 1. (**a**) A double-pass iCMHX design showing cross-media approach; (**b**) planar views showing staggered configuration; (**c**) planar views showing simplified heat transfer domain.

iCMHX is designed to possess similar size and performance as the conventional and standard all-in-one CPU coolers that are typically attached with 120-millimeter standard fans [27,28]. In the current study, iCMHX is compared with one such off-the-shelf conventional unit, an aluminum HX with louver fins on the air side and plain channels on the liquid side, as shown in Figure 2.

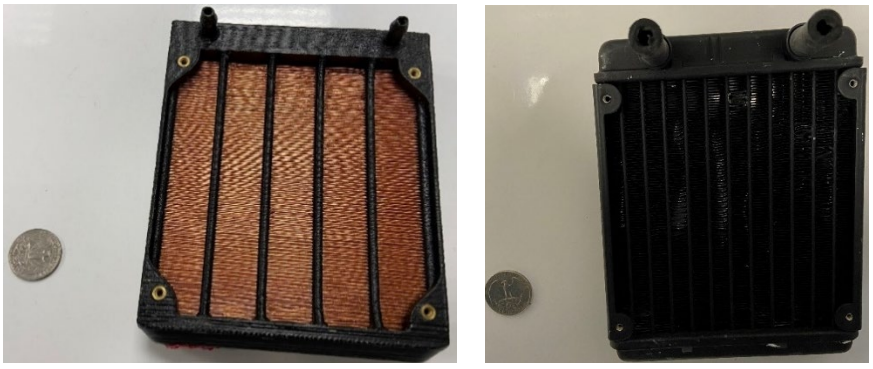

(**a**) (**b**)

Figure 2. (**a**) Additively manufactured iCMHX and (**b**) conventional CPU radiator.

The next section discusses the experimental study, which is later used to validate the numerical model.

2. Experimental Study

The experimental study involves test setup, instrumentation, data reduction, and uncertainty analysis.

2.1. Test Setup

The schematic of the test setup consists of two loops: the air-side loop and the water-side loop, as shown in Figure 3.

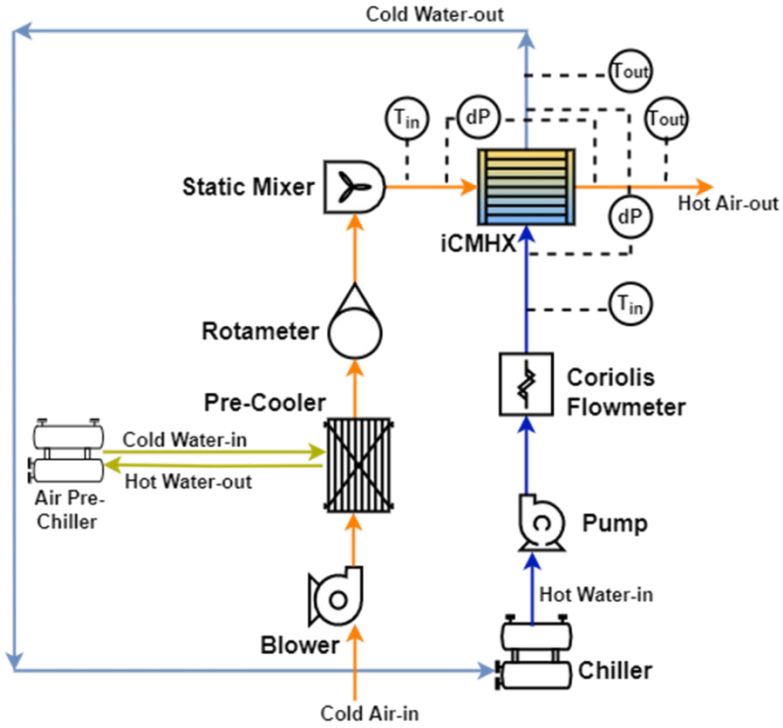

Figure 3. Schematic of the test loop.

The air side is an open loop comprising of a blower, air pre-chiller, pre-cooler, rotameter, and static mixer. The loop starts with a blower that drives room air inside a foam-insulated duct system. The airflow rate inside the duct is varied manually by using a variable frequency drive connected to the blower. The room air then flows past the pre-cooler, which first cools the air coming from the blower to control and reduce air-side inlet temperature. The pre-cooled air then moves across the rotameter, which measures the air flow rate. Air then flows through the duct until it reaches a static mixer that is placed right before the test section to provide uniform temperature distribution entering iCMHX. The air then passes through the test section and exits into the room in an open loop.

Air-side temperatures and pressure drop across HX are measured by thermocouples and analog pressure gauges, respectively. Temperatures of inlet and outlet air are measured by a group of 10 thermocouples, of which each pair of parallel thermocouples is used as one thermopile. Taken together, the 10 thermocouples are arranged in a 10-point mesh structure and placed at the inlet of the test section. The parallel thermocouples reduce temperature uncertainties due to averaged temperature readings over 10 thermocouples as compared to an individual reading [29]. Similarly, outlet air temperature is measured by using another 10 thermocouples with similar thermopile combinations arranged in another 10-point mesh and placed at the outlet of the test section. The temperature grid is placed at locations containing well-mixed airflow for maximum uniformity in temperature. Air-side pressure-drop is measured by an analog pressure gauge, which takes differential readings between the inlet and outlet of HX. The pressure reading at both inlet and outlet is area-averaged via four pressure ports, each located at the inlet and outlet of iCMHX.

The liquid side is a closed loop that includes a chiller, pump, and Coriolis-flowmeter. The loop starts with a chiller that regulates inlet water temperature. Hot water flows via a flexible plastic tube across a pump controlled by user-input voltage defined in LABVIEW. The water then flows through the Coriolis-flowmeter, which measures the liquid-side flowrate before passing through the HX inlet. Subsequently, cold water exits via the HX outlet and flows into the sink of the chiller. The water then continues to run in the closed-loop cycle.

Similarly, the water-side temperatures and pressure drop across the HX are measured by thermocouples and a manometer, respectively. The water temperature of the inlet HX is measured by a group of five thermocouples, of which parallel combinations of two and three thermocouples are used as two separate thermopiles. Similarly, the outlet temperature is measured using another five thermocouples.

2.2. Instrumentation

The instruments used in the test setup are calibrated as listed in Table 1.

Table 1. Technical specifications of measuring instruments.

Fluid	Equipment	Specifications	Uncertainty (±)
Water side	Chiller	ThermoNESLAB RTE 7 (R134A) 800 W heater −25 °C to 150 °C	NA
	Pump	Micropump I-Drive (Type 76,003) 0 to 12.33 g/s	NA
	Coriolis Flowmeter	Endress+Hauser Promass 83 A Nominal Diameter: 1/12″ 0 to 27.7 g/s	0.1% of measured value
	Manometer	0 to 17.85 kPa	50 Pa
	Parallel Thermopile	Omega T-type thermocouples −250 °C to 350 °C	0.22 °C
Air side	Blower	Baldor Industrial Motor—3Phase (F198 series) 0 to 89 g/s	NA
	Pre-Chiller	Forma Scientific Model 2067 650 W heater −20 °C to 70 °C	0.02 °C
	Rotameter	Fischer & Porter (Model No. 10A4557S) 0 to 32 g/s	0.3 g/s
	Analogue Pressure Gauge	Magnehelic Dyer Instruments 0 to 64 Pa	1.25 Pa
	Thermopile Parallel	Omega T-type thermocouples −250 °C to 350 °C	0.16 °C

The test setup is built for operating conditions similar to those of a CPU radiator in liquid cooling applications, as shown in Table 2. Air-side testing includes variable airflow rate ($\dot{m}_a$) with a specified range and a constant waterflow rate ($\dot{m}_w$) kept to its maximum value. Similarly, water-side testing includes variable waterflow rate with specified range and a constant airflow rate. A LABVIEW program connected to a DAQ recorded the testing data.

Table 2. Operating conditions for the experiment.

	iCMHX		Conventional Unit	
Temperature Conditions				
T_a^{in} (°C)	12.8–16.6		12.5–15.4	
T_w^{in} (°C)	42.4–45.5		44–48	
Flow Conditions				
	Air-side Test	**Water-side Test**	**Air-side Test**	**Water-side Test**
$\dot{m}_a$ (g/s)	10–30.8	21.9	12–29	29.2
$\dot{m}_w$ (g/s)	9.5	3.5–9.5	9.6	3.6–9.6

2.3. Data Reduction

The thermal and hydrodynamic performance of iCMHX is quantified by derived parameters, such as heat transfer rate, pumping work, and measured parameters, such as air-side and water-side pressure drops. Thermal and hydrodynamic performances are obtained independently for both air-side and water-side testing data using the procedure described below.

First, heat transfer rates from both the air side and water side are derived from measured flowrates, temperatures, and specific heat capacities C_p, as shown in Equations (1)–(3).

$$Q_a = C_a\left(T_a^{out} - T_a^{in}\right) \tag{1}$$

$$Q_w = C_w\left(T_w^{in} - T_w^{out}\right) \tag{2}$$

Here, C_a and C_w are defined by Equation (3):

$$C_i = (\dot{m}C_p)_i \tag{3}$$

where index i takes the value of a and w.

In order to maintain energy balance (EB) between air and water, EB is computed from the average heat transfer rate, as shown in Equations (4) and (5). For the present study, all experimental data are taken at steady-state, and EB was found to be within 2.3%.

$$Q = \frac{Q_a + Q_w}{2} \tag{4}$$

$$EB\ [\%] = \frac{|Q_w - Q_a|}{Q_{avg}} \times 100 \tag{5}$$

Lastly, total pumping work performed on fluids is computed from measured Δp_a and Δp_w values, as shown below.

$$P_{pumping} = \frac{\dot{m}_a}{\rho_a}\Delta p_a + \frac{\dot{m}_w}{\rho_w}\Delta p_w \tag{6}$$

2.4. Uncertainty Analysis

During any experiment, in-built instrumental uncertainties (α_{x_i}) not only affect measured raw data (x_i) but also induce uncertainties (α_f) on each derived quantity (f_i). The list of random instrumental uncertainties can be found in Table 1. However, in order to obtain uncertainties on derived quantities, an uncertainty analysis was carried out, which uses

the dependence of derived quantities on measured quantities $\left(\frac{\partial f_i}{\partial x_i}\right)$, as explained in NIST Technical Note 1297 [30]:

$$\alpha_{f_j} = \sqrt{\sum_{i=1}^{n}\left\{\left(\frac{\partial f_j}{\partial x_i}\right)^2 \alpha_{x_i}^2\right\}} \quad (7)$$

where x refers to the uncertainties from n different raw measured values including $\dot{m}_w$, $\dot{m}_a$, Δp_a, Δp_w, T_w^{in}, T_w^{out}, T_a^{in}, and T_a^{out}; and α_f includes uncertainty computed for any jth derived quantity such as Q_w, Q_a, ΔT, and $P_{pumping}$. Calculated uncertainties are summarized in Table 3. Here, ΔT is defined as $\Delta T = T_{in}^{w} - T_{in}^{a}$.

Table 3. Calculated uncertainties for key pressure-drop and heat transfer parameters.

Derived Quantities	Calculated Uncertainty (±)
$\mathbf{Q_w}$	1.8–3%
$\mathbf{Q_a}$	1.7–2.6%
$\frac{\mathbf{\Delta T}}{\mathbf{Q}}$	1.1–2.2%
$\mathbf{P_{pumping}}$	3.3–12%

3. Effect of Printing Variabilities

Before we developed the numerical model, we studied the effect of printing variabilities on iCMHX dimensions due to additive manufacturing. This is the first time such a study has been conducted for any cross-media HXs. For this study, iCMHX was first hardened using an Allied epoxy-set of resin and hardener to retain its original dimensions and then machined into different segments (see Figure 4), which were analyzed using Keyence VR3200 microscope and Hitachi SU-70 FEG SEM.

Some major printing variabilities are discussed below:

- The wires were extremely squashed in the water flow direction (y axis), such that they acquired spatially varying ellipsoidal shapes instead of nominal circular shapes (see Figure 4a). This could be due to improper functioning of the wire-extruder mechanism of the printer's metal head.
- The wire spacings, particularly S_L, varied with a high standard deviation, which is evident in Figure 4a. This misalignment among a few rows of wires deviated from the nominal staggered configuration and might have occurred due to precision errors in the movement of the printer's metal head.
- Water channel width, W_w, also varied spatially due to variable polymer wall thickness (see Figure 4b), which is possibly caused by precision errors in the movement of the printer's polymer head. The deviation in the average reading of the width of the water channel from its nominal reading was the highest of all geometrical parameters.
- The coating thickness of polyurethane sealant (t_{coat}) around the wire was measured to be around 20 μm.

A statistical analysis on the measured dimensions was carried out, and the summarized dimensions are shown in Table 4.

Based on average measured dimensions, overall iCMHX design parameters (see Figure 1) are formulated, as shown in Table 5. The table also includes the design details of the conventional CPU radiator (see Figure 2b) as measured.

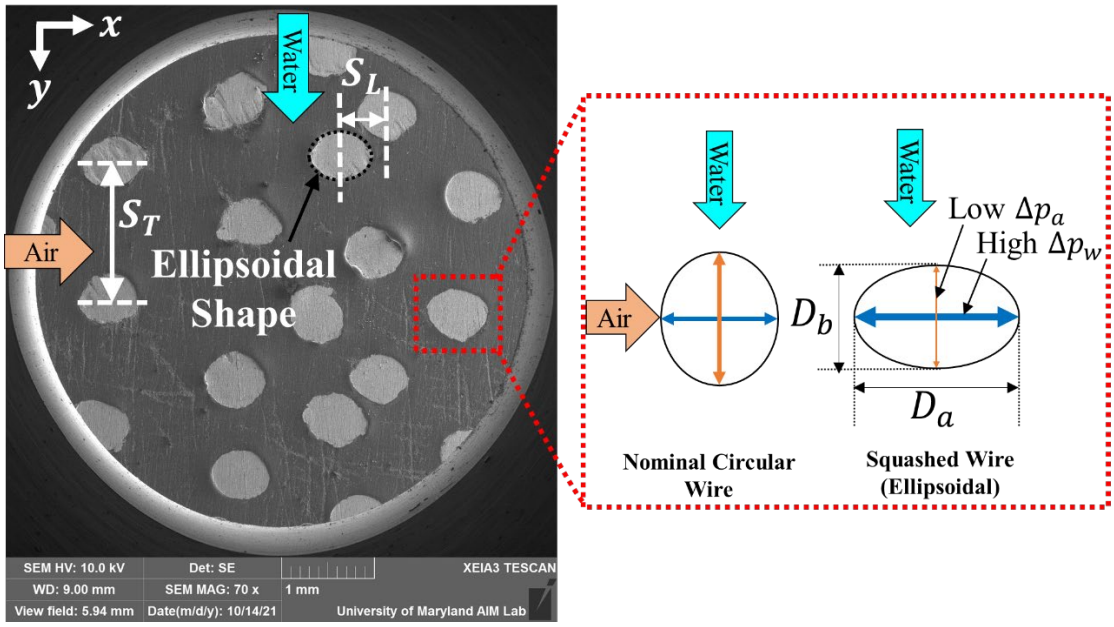

(**a**)

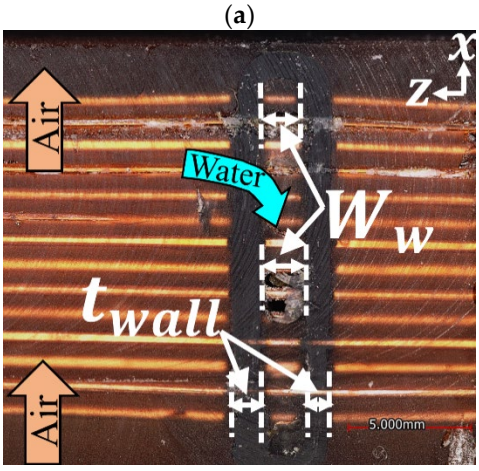

(**b**)

Figure 4. (**a**) SEM image for wire spacings and wire shape and (**b**) microscope image of varying water channel width.

Table 4. Measured dimensions of iCMHX due to printing variabilities.

	Nominal	Measured			
	(mm)	Average (mm)	Standard Deviation (mm)	Range (mm)	Number of Measurement Points
D_a	0.44	0.48	0.042	0.343–0.686	982
D_b	0.44	0.42	0.045	0.275–0.566	1025
S_T	1.4	1.4	0.15	0.472–2.78	941
S_L	1	0.94	0.253	0.224–1.74	850
W_w	2	1.79	0.18	1.23–2.13	106
t_{wall}	1	1.08	0.127	0.85–1.48	49

Table 5. Design details, as measured, of the current iCMHX unit and conventional CPU radiator.

	iCMHX	Conventional CPU Radiator
Overall design		
$\mathbf{L_a}$ $(\mathbf{mm})$	16	15
$\mathbf{L_w}$ $(\mathbf{mm})$	119.6	118
$\mathbf{L_{nf}}$ $(\mathbf{mm})$	119	109.75
$\mathbf{m_{HX}}$ $(\mathbf{mm})$	253.2	
$\mathbf{Vol_{HX}}$ $(\mathbf{mm^3})$	2.27×105	
Polymer geometrical parameters		
$\mathbf{W_a}$ $(\mathbf{mm})$	19	7.23
$\mathbf{W_w}$ $(\mathbf{mm})$	1.79	1.9
$\mathbf{t_{wall}}$ $(\mathbf{mm})$	1.08	0.13
$\mathbf{nc_a}$	5	12
$\mathbf{nc_w}$	6	13
Fin geometrical parameters		
$\mathbf{S_T}$ $(\mathbf{mm})$	1.4	1.241
$\mathbf{t_{fin}}$ $(\mathbf{mm})$	-	0.2
$\mathbf{S_L}$ $(\mathbf{mm})$	0.9	-
$\mathbf{D_a}$ $(\mathbf{mm})$	0.48	-
$\mathbf{D_b}$ $(\mathbf{mm})$	0.42	-
$\mathbf{N_T}$	14	-
$\mathbf{N_L}$	84	94

By using the above dimensions, the numerical study is then carried out in the next section.

4. Numerical Study

The numerical study comprises 3D CFD-based simulations at the segment-level and an analytical-based model at the entire HX level. This is the first time such a modeling approach has been adopted innovatively for cross-media HXs containing finned surfaces on both air and water-side channels. This approach saves computational time as only segment-level based CFD simulations are performed instead of entire HX-based simulations. This computational advantage offered by the present numerical model might also be useful for design optimization of HXs in the future. The segment-level based 3D CFD study is performed on ellipsoidal shaped wires or tube-banks. Although several studies have been performed on ellipsoidal shaped tube-banks [31–36], limited studies have been performed that are directly relevant to the current study's elliptical eccentricity, tube-bank spacing parameters, and laminar flow conditions.

From the flow path shown in Figure 1, the hot liquid representing heat carried from the CPU enters the iCMHX inlet, where it becomes divided into half of the total liquid channels ($nc_w/2$); it is separated from the other half of the channels via a thin polymer wall located in the top manifold. The inlet liquid traverses downward in the y direction and then mixes at the bottom manifold before flowing up in the other half of the liquid channels in the y-direction, facilitating a double-pass liquid-flow. Simultaneously, cold air flows pass iCMHX across nc_a air channels in the x crossflow direction. Due to the temperature difference between the fluids ($\Delta T = T^w_{in} - T^a_{in}$), heat is transferred between hot liquid and cold air, as shown in the thermal circuit diagram for a given wire in Figure 1c. Extending the thermal circuit analogy for the entire iCMHX, R_{total} is formulated as shown in Equation (8).

$$R_{total} = R_a + R_w + R_{cond} \quad (8)$$

Thus, in order to compute overall HX resistance, convective (R_a, R_w) and conductive thermal resistances (R_{cond}) present in iCMHX need to be determined. However, resistances can only be determined if convective heat transfer coefficients on the air and water sides are known. Thus, a simplified 3D CFD model for ellipsoidal tube-banks is created for both

air-side and water-side domains to obtain air-side and water-side heat transfer coefficients. The 3D CFD better captures the boundary effects than a 2D model. This model is also used to determine air-side and water-side pressure-drop values. Once the performance parameters from the 3D CFD model are obtained, R_{total} of the entire HX can be then computed analytically.

4.1. 3D CFD Model

As shown in Figure 1a, the entire HX model domain consists of nc_w water channels and nc_a air channels separated by polymer walls. One method to obtain convective fluid heat transfer coefficients is by determining the Nusselt number of the fluids (Nu_a and Nu_w), as explained in the literature [36,37]. Since the Nusselt number is dependent only on flow and geometric conditions, representative air-side and water-side domains can be modeled independently and separately to obtain respective fluid heat transfer coefficients.

The water-side domain for the current study is obtained by simplifying one of the water channels of the iCMHX, as shown in Figure 5a,b.

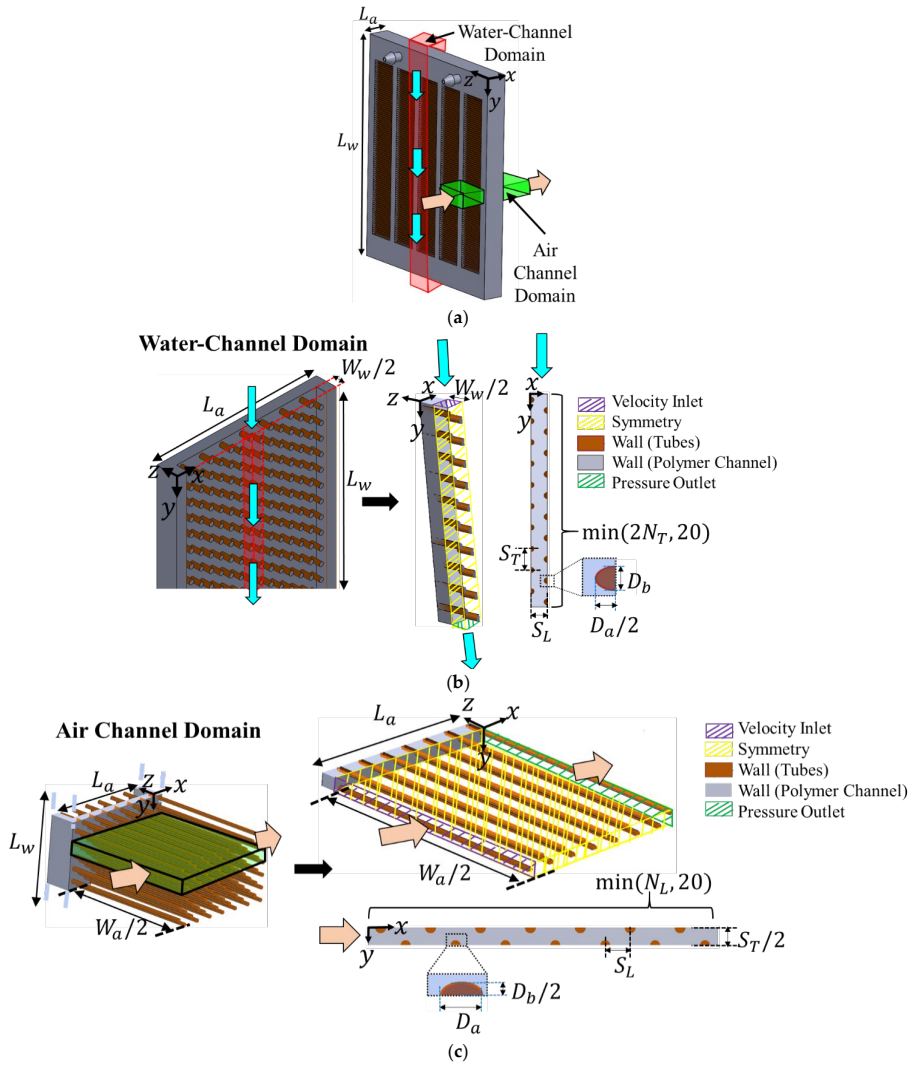

Figure 5. Domain simplifications: (**a**) entire iCMHX domain; (**b**) simplification to water-side domain; and (**c**) simplification to air-side domain.

This is performed by assuming uniform fluid flow and temperature profile across all water inlets. As shown, the water-side domain is first reduced from a single water channel to a single symmetrically half water channel consisting of $L_a \times W_w/2 \times L_w$ dimensions. The

3D domain, however, can be further reduced along L_a and L_w dimensions. A symmetric flow field is expected along the y-direction for given flow ranges ($30 < Re_w < 80$, see nomenclature), as similarly observed in the literature [38]. Thus, L_a dimensions, including N_L wires, can be reduced to a symmetric domain consisting of two consecutive wires in the x-direction S_L distance apart. The effect of the wall boundary in the x-direction is modeled separately by using similar domain and boundary conditions. For the L_w dimension, the computational domain in the y-direction can be reduced by using at least 20 wires, as the equivalent number of wires in the longitudinal direction to waterflow ($2N_T$) is too large. These equivalent wires are defined based on longitudinal spacing between the wires ($S_T/2$) along the waterflow direction. Since the water channels are too narrow, the ratio of width of the water-channel (W_w) to transverse spacing between the wires ($2S_L$) is much less than 5; therefore, the velocity component and gradients of the velocity field of the water flow in the z direction cannot be neglected, as explained in the literature [17]. Thus, the wall boundary condition on the polymer wall must be modeled.

Similarly, the air-side domain can be obtained from one of the air channels of the entire iCMHX, as shown in Figure 5a,c. As shown, the air-side domain is first reduced to a single symmetrically half air channel consisting of $L_a \times W_a/2 \times L_w$ dimensions. As the airflow is also expected to have a symmetric flow field in the x-direction for given flow ranges ($25 < Re_a < 70$, see nomenclature), the 3D domain is then further reduced along L_w dimensions, including N_T wires, to a symmetric domain consisting of two consecutive wires in the y direction at $S_T/2$ distance apart. The rest of the other dimensions can be simplified. Since the air channels are too wide ($W_w/S_T >> 5$), the wall boundary condition in the z direction might not be needed. However, for consistent boundary conditions, it is modeled as a 3D domain, such as the water side.

Both air-side and water-side computational domains are created in Gambit software using MATLAB scripting. Each computational domain is obtained by first using edge-meshing operation along with mesh-refinement on the wire edges, followed by face meshing operation on the surface using triangular elements and pave scheme. Later, hexahedral and wedge type elements along with cooper scheme suitable for cylindrical surfaces, are used to mesh the entire domain volume.

A velocity inlet condition is imposed on the surfaces where the fluids enter their respective domains, while a pressure-outlet condition of zero Pa is imposed on surfaces where the fluids exit the domains. In order to ensure that the upstream and downstream boundary conditions do not affect the results, the inlet and outlet are kept at around $11D_h$ from the first and last wires, as is performed in the authors' past study [23]. A temperature Dirichlet wall-boundary condition is imposed on the ellipsoidal wires. Some constant temperatures can be considered at the inlet and the wires as temperature does not affect the Nusselt number, assuming that thermophysical properties are constant. The meshed domains are separately simulated in Ansys Fluent for different flow velocities, v_b, with assumptions and solver details mentioned in Table 6.

Table 6. Assumptions and solver details.

Assumptions
Laminar flow, steady-state, incompressible flow
Constant fluid and material properties
Uniform fluid flow and temperature profiles at the inlets
Solver Details and Methods
PRESTO for pressure
1st order upwind for momentum and energy
Coupled scheme for pressure and velocity
Convergence tolerance : 10^{-6} for continuity and momentum; 10^{-14} for energy

Flow velocities are calculated from flowrates, as shown in Equations (9)–(11):

$$A_a^{flow} = W_a(nc_a)S_T N_T \tag{9}$$

$$A_w^{flow} = W_w(nc_w/2)S_L N_L \tag{10}$$

$$v_{bi} = \frac{\dot{m}_w}{\rho_i A_i^{flow}} \tag{11}$$

where index i takes the value of a and w.

For thermal performance, Nusselt numbers for both fluids are obtained using the Eff-NTU method as detailed in [23]. Typical velocity and temperature contour plots at some given flow rate for the air-side domain are shown in Figure 6.

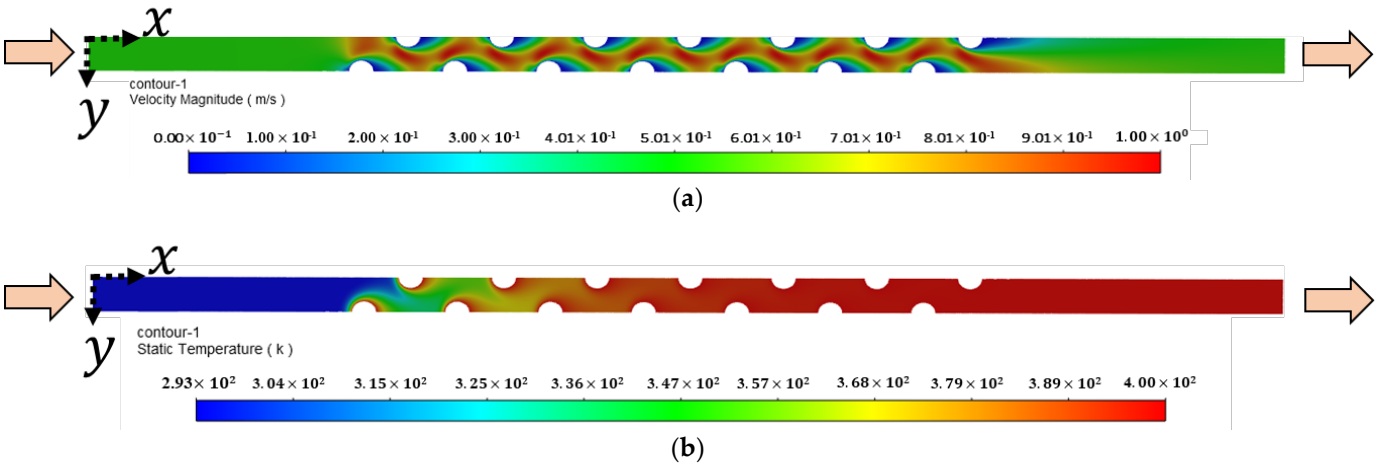

Figure 6. Contour plots of (**a**) velocity and (**b**) temperature for some particular flow-rate at symmetry plane of the air-side domain located $W_a/2$ distance from the wall.

Once Nu_a and Nu_w are obtained based on the geometric parameters such as, D_h, S_T, and S_L and flow parameters such as Reynolds number and fluid heat transfer coefficients for both air and water are determined from Equation (12). The definition of D_h is based on circular area ($\pi D_h^2/4$) equivalent to the actual ellipsoidal area ($\pi D_a D_b/4$) (see Figure 4a):

$$h_i = \frac{Nu_i k_i}{D_h} \tag{12}$$

where index i takes the value of a and w..

Similarly, for hydrodynamic performance, Euler numbers are obtained for both the fluids based on the total number of wires simulated and v_b. A detailed analysis can be found in [23].

Furthermore, to check the independence of the CFD results from convergence tolerances and mesh sizes, a residual independence study is carried out, followed by a mesh independence study. For the residual independence study for a given mesh, continuity residuals are varied from 10^{-5} to 10^{-6} and the Euler and Nusselt numbers are observed to vary within 0.02%. For the mesh-independence study, residual independent values of Euler and Nusselt numbers are used for a given mesh. Mesh cells are varied uniformly in all x-directions, y-directions and z-directions. For the air side, as mesh cells vary from 880,000 cells to about 2,100,000 cells, Eu_a and Nu_a are found to vary within 0.7%. Similarly, for the water side, as mesh cells vary from 340,000 cells to about 3,600,000 cells, Eu_w and Nu_w are found to vary within 2%.

A graphical representation of CFD-obtained convective heat transfer coefficients (h_a and h_w) is shown in Figure 7.

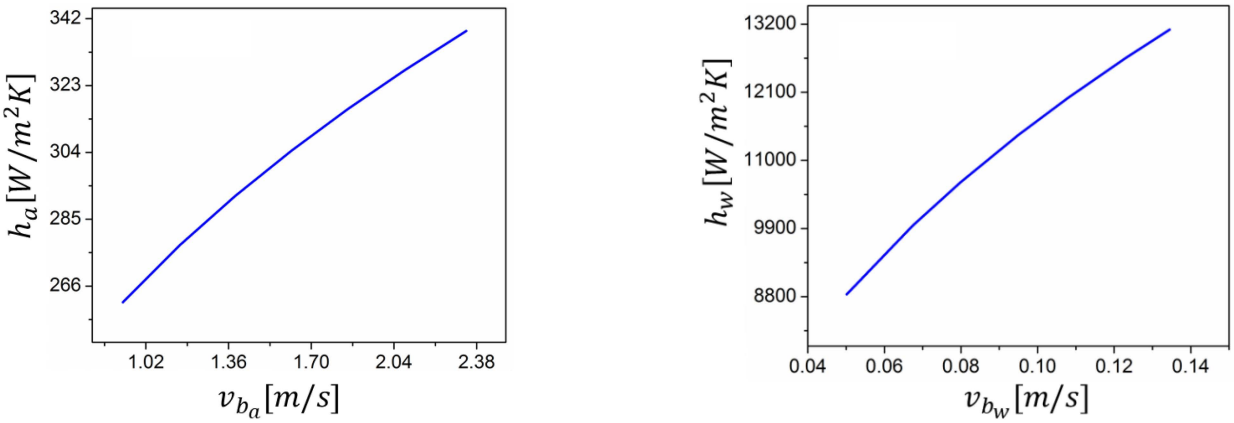

Figure 7. Convective heat transfer coefficients obtained from 3D CFD based on Equation (12) for (**a**) air side and (**b**) water side.

4.2. Analytical Model for the Entire HX

For overall HX thermal performance, h_i computed from Equation (12) can be used analytically to compute R_a and R_w based on the total heat transfer area of the entire HX. However, there is also an additional convective resistance due to the polyurethane coating on the wire. The resulting heat transfer coefficient due to the coating can be defined based on cylinder thermal resistance, as defined in the literature [37] and shown in Equation (13). It is computed to be around 11,483 W/m^2K.

$$h_{coat} = \frac{2k_{coat}}{D_h \log\left(\frac{D_h/2+t_{coat}}{D_h/2}\right)} \tag{13}$$

The effective heat transfer coefficients can, thus, be calculated as shown below:

$$\frac{1}{h_{effi}} = \frac{1}{h_i} + \frac{1}{h_{coat}} \tag{14}$$

$$R_i = \frac{1}{h_{effi} A_i^{fins} \eta_i} \tag{15}$$

where index i takes the value of a and w.

Here, fin-efficiency (η_i) is computed with adiabatic fin-tip assumption [37], as shown in Equations (16)–(18).

$$m_i = \sqrt{\frac{4h_{effi}}{k_{wire} D_h}} \tag{16}$$

$$L_i^c = \frac{w_i}{2} \tag{17}$$

$$\eta_i = \frac{\tanh(m_i L_i^c)}{m_i L_i^c} \tag{18}$$

The total fin-heat transfer area for the entire HX is estimated as shown below:

$$A_i^{fin} = \pi D_h w_i N_a^{fins} N_w^{fins} nc_i \tag{19}$$

where index i takes the value of a and w.

Furthermore, conductive resistance is computed analytically from Equation (20), and R_{total} can now be obtained from Equation (8):

$$R_{walls} = \frac{t_{wall}}{k_{wire} A_{wire}^{CS}} \tag{20}$$

where $A_{wire}^{CS} = (2 \times nc_w) \times \pi \frac{D_h^2}{4} N_a^{fins} N_w^{fins}$.

The total heat transfer rate is now obtained by using the Eff-NTU method for the entire HX for crossflow configuration for both fluids unmixed [37], as shown in Equations (21)–(26).

$$UA_{overall} = \frac{1}{R_{total}} \tag{21}$$

$$C_{min} = \min\{C_a, C_w\} \tag{22}$$

$$NTU_{overall} = \frac{UA_{overall}}{C_{min}} \tag{23}$$

$$C_r = \frac{C_{min}}{C_{max}} \tag{24}$$

$$\varepsilon_{HX} = 1 - e^{\frac{1}{C_r} NTU_{overall}^{0.22} (e^{-C_r NTU_{overall}^{0.78}} - 1)} \tag{25}$$

$$Q = \varepsilon_{HX} C_{min} \Delta T \tag{26}$$

Similarly, for the overall hydrodynamic performance of HX, Eu_a and Eu_w obtained from CFD in the previous section are used analytically as shown below:

$$\Delta p_a = \frac{1}{2} \rho_a v_{b_a}^2 N_L Eu_a \tag{27}$$

$$\Delta p_w = \frac{1}{2} \rho_w v_{b_w}^2 (2N_T) Eu_w \times 2 \tag{28}$$

where $2N_T$ represents the effective number of wires in the longitudinal direction to the waterflow rate, while the other multiplicative factor of 2 corresponds to the double-pass waterflow.

5. Results and Discussion

This section validates the numerical study using experimental results for both water-side and air-side testing. The present numerical study is further compared with the authors' past numerical work [23,24].

5.1. Validation of Numerical Results with Water-Side Testing Data

Water-side testing is based on the test data showing an energy balance of up to ±1.5%. Thermal performance is tested by varying water-side flowrate on a normalized thermal parameter, $\Delta T/Q$, as shown in Figure 8. It is observed that as flowrate increases, $\Delta T/Q$ decreases in an inverse power law form. This is because the increasing flow rate increases the water-side heat transfer coefficient (h_w) or decreases R_w (see Equation (15)). This further reduces overall thermal resistance, which is proportional to $\Delta T/Q$. A 168% increase in the water-side flowrate results in about 26% decrease in $\Delta T/Q$. The experimental results are further validated with the present numerical approach, and a match well within 8% is observed. The present numerical approach is also comparable to the authors' past numerical work based on nominal design and excludes the effects due to coating, wall-boundaries in x and z-directions (see Figure 5) and dimensional changes due to printing variabilities. The combined effects due to dimensional changes and wall-boundaries on the water-side parameters such as Nusselt number (Nu_w) are more significant than that on the air-side. Water-side dimensional changes such as reduced water-channel width (W_w) and reduced transverse fin-spacing-ratio on the water-side ($2S_L/D_h$), result in a net 20% higher v_{b_w} than nominal. This significantly increases the water-side Nusselt number

as compared to the past numerical work and as typically observed in the literature [39]. The Nusselt number inside the channels is further increased due to augmented flow and thermal field due to the wall-boundaries. Thus, considering all net wall and dimensional effects, water-side resistance (R_w) is expected to decrease or the heat transfer coefficient (h_w) is expected to increase significantly as compared to the past numerical study. Now, to compute the effective water-side resistance, coating resistance is then included. This coating effect, however, greatly reduces the effective heat transfer coefficient on the water-side (h_{eff_w}) to half of the value obtained due to dimensional changes (h_w) because h_w is comparable to = coating heat transfer coefficient (h_{coat}) in magnitude (see Equation (14)). This results in an effective increase in R_w by 18 to 23% as compared to the past numerical study. Similarly, the combined effects due to dimensional changes and wall-boundaries affect air-side parameters but to a lesser extent as the air-side dimensions do not deviate much from the nominal. Thus, considering all net effects, air-side thermal resistance (R_a) is also expected to slightly decrease. Further inclusion of coating effect, however, does not affect R_a as $h_{coat} >> h_a$. This results in an effective decrease in Ra, as expected, to about 5–5.2% than nominal. The total resistance (R_{total}), which is majorly dominated by the air-side as R_a constitutes about 63–77% of the total resistance (Equations (8) and (15)), is found to be comparable to the past numerical study to within 0.4%.

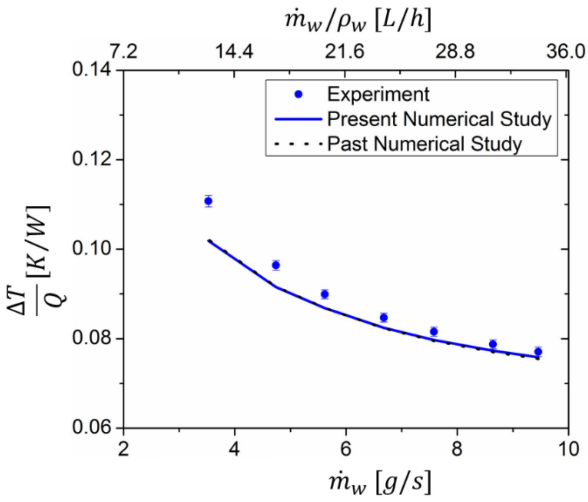

Figure 8. Comparison of experimental and numerical results of ΔT/Q for different $\dot{m}_w$.

The hydrodynamic performance, Δp_w, is measured directly. However, Δp_w includes the pressure drop from the connecting flexible plastic tubes, the integrated top-bottom liquid-side manifolds, and the HX core. Thus, Δp_w^{core} across the test section can be obtained by subtracting the extra pressure drop due to tubes and manifolds from measured Δp_w values, as mentioned in the authors' past study [24]. HX core pressure drop is observed to increase with the increasing flow rate in a quadratic manner, as shown in Figure 9.

The present numerical study also matches experimental results to within 17.8%. The deviation increases with an increase in water-side flowrate due to losses associated with v_w^2 (see Equation (28)). The present numerical approach significantly outperforms the past numerical study, which includes the effects of wall-boundaries and water-side dimensional changes. As dimensional changes result into 20% higher velocity of water than the nominal, a higher pressure drop is expected, as observed in the literature [40]. To add to this, the squashed fin-shape on the water-side (see Figure 4a) also results in higher pressure-drop than nominal. In addition to these dimensional changes, the wall-boundary effects in x and z-directions (see Figure 5b) were not considered in the symmetric 2D CFD model of the past numerical study. Since there are a small number of N_L wires in the x-direction, the viscous effects of the boundary layer along the wall are not quantified in the past numerical study. It is observed that, along the x-direction, a thick boundary layer was developed near

the walls due to small spacings between the wall and the nearest wires in the x direction, S. This causes the flow to choke around those wires (see Figure 10), resulting in about 17% increase in Δp_w^{core}. In order to avoid choking the flow, spacing should be increased (S′) in the future. However, in practice, an optimal spacing should be selected, as large spacing can cause flow bypass. Similarly, due to narrow water channels, the wall-boundary effect in the z-direction alone results in almost 35% increase in Δp_w^{core} as compared to the past numerical study.

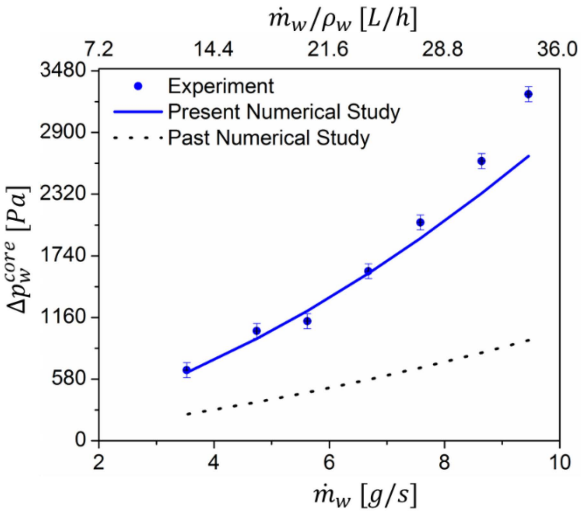

Figure 9. Comparison of experimental and numerical results of Δp_w^{core} for different $\dot{m}_w$.

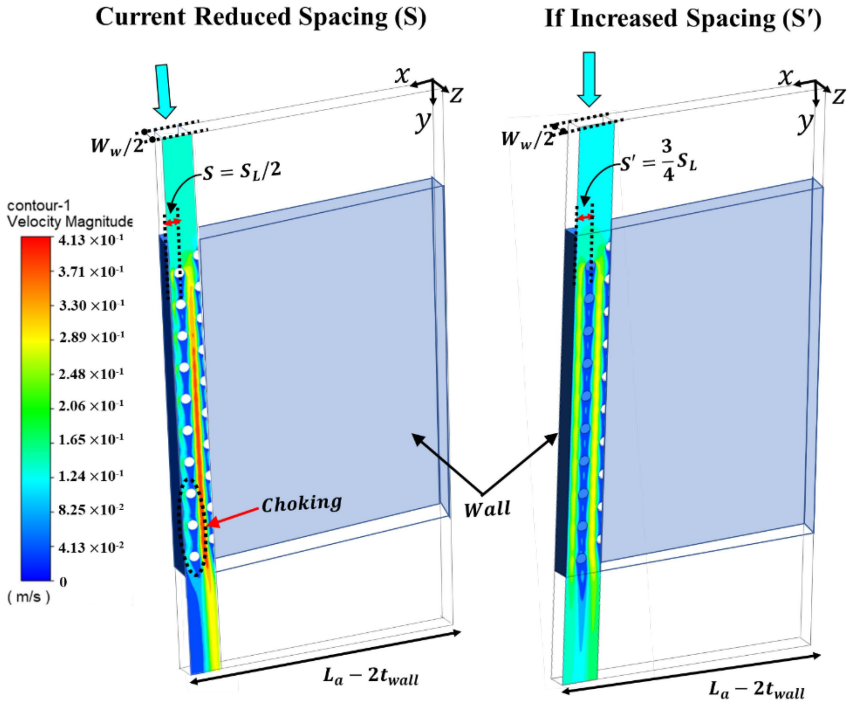

Figure 10. Choking effect around the nearest wires to the wall due to small spacing (S) (on **left**) and no-choking effect around those wires if S is increased (S′) (on **right**) at some particular flow-rate.

5.2. Validation of Numerical Results with Air-Side Testing Data

Similarly, air-side testing data are based on test data exhibiting an energy balance of within ±2.3%. Thermal performance is studied by the effect of varying airflow rate on $\frac{\Delta T}{Q}$, as shown in Figure 11. As $\dot{m}_a$ increases, $\frac{\Delta T}{Q}$ also decreases in the inverse power law form

due to decreasing R_a. About 153% increase in airflow rate results in about 35% decrease in $\frac{\Delta T}{Q}$. The testing results are further compared with the present numerical model and match well within 4.16%. Compared with Figure 8, Figure 11 provides a steeper slope, which confirms the earlier reasoning that the air-side is the limiting side due to $R_a \gg R_w$. These results are comparable with the past numerical study. This can be explained based on the cumulative effect in R_a due to coating and dimensional changes, resulting in comparable thermal performances, as discussed in the previous section.

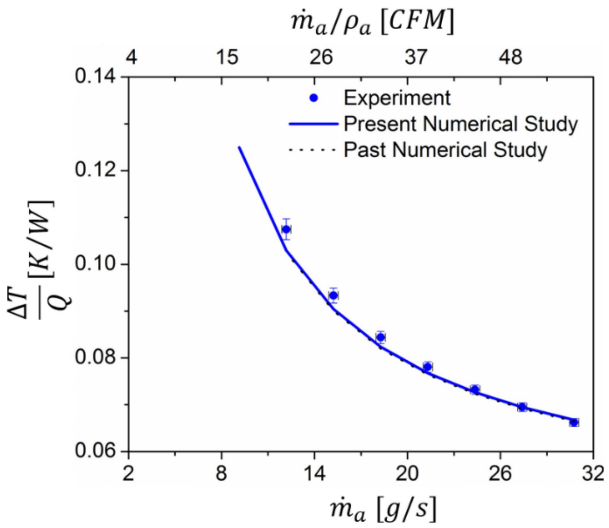

Figure 11. Comparison of experimental and numerical results of $\Delta T/Q$ for different $\dot{m}_a$.

Similarly, the hydrodynamic performance of the air side, Δp_a, is observed to increase with increasing airflow rates approximately quadratically, as shown in Figure 12, matching with the trends observed in the literature [38,41]. The air-side pressure drop also seems to match reasonably well with the present numerical study for low flow-rate points. However, for higher flow-rate points, numerical predictions slightly overpredict experimental results to within 11.7%, which could be due to amplified losses associated with v_a^2 for higher flowrates (see Equation (27). The present model also deviates from the past numerical study, which could be due mainly to dimensional changes such as 4.5% contraction in ellipsoidal shape on the air-side as compared to that of the nominal circular shape (see Figure 4a) considered in the past study. This results in smaller wake regions, resulting in reduced pressure drop [42], as compared to the past numerical study.

5.3. Comparison to a High-Performance, Commercially Available CPU Cooler Radiator

iCMHX performance was compared with that of a conventional, high-performance metallic CPU radiator for low temperature and pressure applications. The conventional, commercially available unit was experimentally tested in the same test setup and similar testing conditions as iCMHX (see Table 2). thermal and hydrodynamic performances of the two HXs were compared. Thermal performance is characterized by $\frac{\Delta T}{Q}$, while hydrodynamic performance is characterized by the total pumping power, $P_{pumping}$. Since the pumping power is dominated mainly by the air side due to its high volumetric flow rate as compared to the waterflow rate, air-side test data were used to compare HX performances. As shown in Figure 13, iCMHX delivers performance comparable to the conventional unit to within 10%, where the ±10% lines are drawn with reference to the conventional unit.

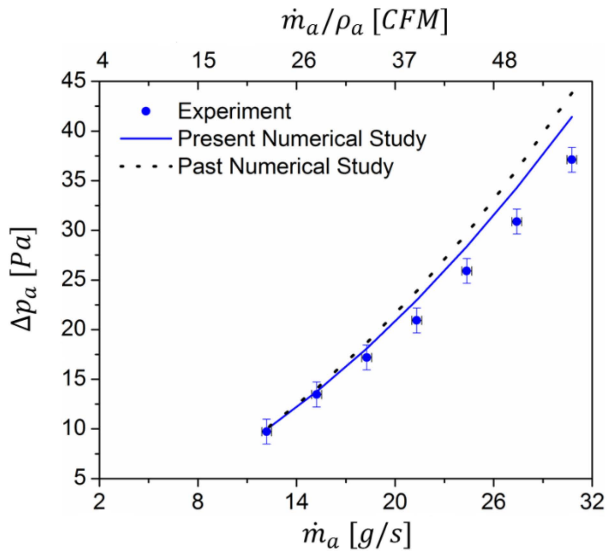

Figure 12. Comparison of experimental and numerical results of Δp_a for different $\dot{m}_a$.

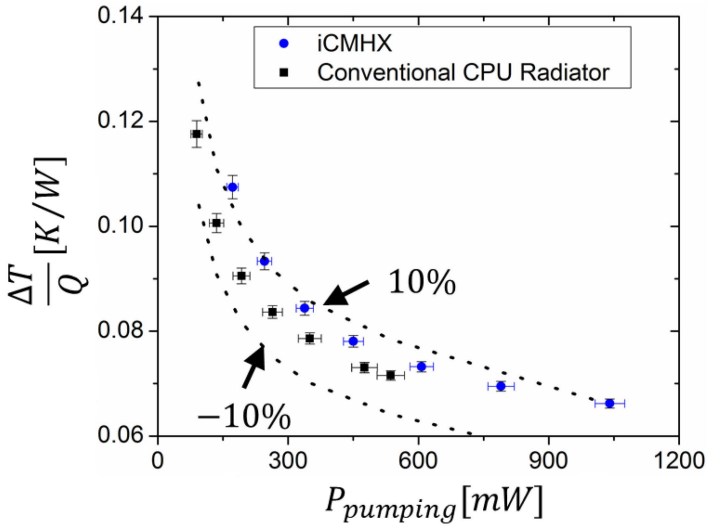

Figure 13. Comparison of experimental ΔT/Q for different pumping powers $P_{pumping}$ for both iCMHX and conventional CPU radiator.

For comparable thermal and hydrodynamic performance, iCMHX offers unique design advantages over conventional HX designs. The robust additive manufacturing technique enables customized and complex yet reliable design solutions, such as the cross-media design introduced here, to offset the penalty introduced due to the low conductivity of polymer. For example, given that the air side of the HX is the limiting side, iCMHXs can be designed with increased air-side heat transfer area, possibly by optimal and controlled squashing of the fins into ellipsoidal and flat-ribbon shapes. These ribbon-shaped fins might, however, further increase the water-side pressure drop. This water-side impedance can be mitigated by designing iCMHX in a counter-flow configuration instead, which would also increase thermal performance over that of the present crossflow configuration. This could be performed by changing the water flow direction via modified water inlet channels.

The digital design and manufacture of the iCMHX will inherently reduce costs and speed its manufacture. In addition to this, there are additional advantages of printing on-site/on-demand, generating additional savings in transportation, and packaging costs.

6. Conclusions

A novel, additively manufactured metal-polymer composite integrated cross-media heat exchanger (iCMHX) was experimentally and numerically studied in the present study. iCMHX was experimentally tested and compared with a metallic-based conventional CPU cooler. In addition to the experimental investigation, the performance of the entire iCMHX was numerically investigated using a robust and simplified 3D CFD and analytically based model. This 3D-CFD model is based on ellipsoidal fins in staggered tube banks ($S_T/D = 3.33$ and $S_L/D = 1.96$) for a laminar regime ($Re < 100$). The iCMHX presented here is the first of its kind to have an integrated manifold system attached to the HX core. Three-dimensional fabrication variances from the actual design and their effect on heat transfer and pressure drops were discussed. It was found that the fin shapes were ellipsoidal instead of the designed nominal circular geometry and that this was due to 9% squashing on the water-side channels during the 3D printing process. The numerical model of the iCMHX is robust and computationally much faster when compared to CFD modeling of the entire iCMHX domain. Experimental thermal performance validation correlates well with the numerical model to within 8% for the tested flow and operating conditions representing the selected CPU cooling application. The air-side pressure drop validates well with the numerical model to within 11.7%. The corresponding water-side pressure drop correlates with the numerical model to within 18%. The two major reasons for higher pressure drop on the water side are believed to be due to 1.7 mm narrow water channels and the small spacing between water-side polymer walls and adjacent wires in the x-direction. The validated numerical model can be also used to obtain optimized design of iCMHX for different applications.

Lastly, the comparison of iCMHX performance with that of a conventional metallic-based CPU cooler suggests great progress in digital 3D fabrication of next-generation polymer composite heat exchangers. These HXs offer important advantages, such as lower cost, customized design and fabrication, on-demand and on-site printing of the HX, and the ability to introduce complex yet reliable design solutions that offset the low conductivity of polymers.

Author Contributions: All the authors contributed to the conceptualization and implementation of the research. G.K. simulated, performed experiments, and analyzed the data. G.K. worked on developing the numerical model under the guidance and supervision of R.K.M., A.S., and M.O. All authors have read and agreed to the published version of the manuscript.

Funding: This research was funded by US Department of Energy, ARPA-E division under award DE-AR0000584.

Institutional Review Board Statement: Not applicable.

Informed Consent Statement: Not applicable.

Data Availability Statement: Not applicable.

Acknowledgments: The authors are grateful to financial support of this project by the U.S. Department of Energy, ARPA-E division. The authors wish to thank David Tew, Geoffrey Short, and Joel Fetter, all from ARPA-E, for their technical insight and advice over the course of this project. The views and opinions of authors expressed herein do not necessarily state or reflect those of the United States Government or any agency thereof.

Conflicts of Interest: The authors declare no conflict of interests.

Nomenclature

A	area, m^2
C	heat capacity, W/K
C_p	specific heat capacity, W/kgK
C_r	the ratio of maximum heat capacity to minimum heat capacity
D	diameter of the wire, m
Eu	Euler number
h	heat transfer coefficient, W/m^2 K
k	thermal conductivity, W/mK
L	length, m
m	fin-parameter
$\dot{m}$	mass flow-rate, kg/s
N	number of fins
nc	number of channels
Nu	Nusselt number
P	pumping power, W
Q	heat transfer rate, W
R	thermal resistance, K/W
Re	Reynolds number $\left(=\frac{\rho v_b D_h}{\mu}\right)$
S	spacing, m
T	temperature, °C
t	thickness, m
UA	thermal conductance, W/K
v_b	free stream velocity, m/s
W	width of channels, m
x	the direction along x axis
y	the direction along y axis
z	the direction along z axis
Greek Symbols	
α	uncertainty
Δp	pressure-drop, Pa
ε	fin effectiveness
μ	dynamic viscosity, kg/ms
η	fin efficiency
ρ	density, kg/m^3
Subscripts	
a	air
avg	average
cond	conductive
eqv	equivalent
f	flow
h	hydraulic
l	longitudinal direction
max	maximum
min	minimum
nf	no flow
o	overall
r	ratio
t	transverse direction
th	thermal
w	water
Superscripts	
c	corrected
cs	cross-section
in	inlet
out	outlet
s	surface

Abbreviations

ABS	acrylonitrile butadiene styrene
COP	coefficient of performance
CPU	central processing unit
DAQ	data acquisition
EB	energy balance
EFCAM	embedded fiber composite additive manufacturing
FDM	fused deposition modeling
HX	heat exchanger
iCMHX	integrated cross-media heat exchanger
NA	not applicable
NTU	number of transfer units
SEM	Scanning Electron Microscope
Vol	Volume

References

1. Qasem, N.; Zubair, S.M. Compact and microchannel heat exchangers: A comprehensive review of air-side friction factor and heat transfer correlations. *Energy Convers. Manag.* **2018**, *173*, 555–601. [CrossRef]
2. Lyu, S.; Wang, C.; Zhang, C.; Royon, L.; Guo, X. Experimental characterization of a novel soft polymer heat exchanger for wastewater heat recovery. *Int. J. Heat Mass Transf.* **2020**, *161*, 120256. [CrossRef]
3. Didmanidze, O.N.; Khakimov, R.T.; Parlyuk, E.P.; Bol'Shakov, N.A. Test Results of a Polymer Radiator of MTZ-80 Tractor Cooling System. *Agric. Mach. Technol.* **2020**, *14*, 55–60. [CrossRef]
4. Chen, X.; Su, Y.; Reay, D.; Riffat, S. Recent research developments in polymer heat exchangers–A. review. *Renew. Sustain. Energy Rev.* **2016**, *60*, 1367–1386. [CrossRef]
5. Githens, R.E. Flexible-tube heat exchangers. *Chem. Eng. Prog* **1965**, *61*, 55–62.
6. Deisenroth, D.C.; Moradi, R.; Shooshtari, A.H.; Singer, F.; Bar-Cohen, A.; Ohadi, M. Review of Heat Exchangers Enabled by Polymer and Polymer Composite Additive Manufacturing. *Heat Transf. Eng.* **2017**, *39*, 1648–1664. [CrossRef]
7. Mark, J. *Physical Properties of Polymers Handbook*; Springer: New York, NY, USA, 2007.
8. Glouannec, P.; Chauvelon, P.; Feller, J.; Noël, H.; Ploteau, J.-P. Current passage tubes in conductive polymer composite for fluid heating. *Energy Convers. Manag.* **2008**, *49*, 493–505. [CrossRef]
9. Xu, Y.; Ray, G.; Abdel-Magid, B. Thermal behavior of single-walled carbon nanotube polymer–matrix composites. *Compos. Part A Appl. Sci. Manuf.* **2006**, *37*, 114–121. [CrossRef]
10. Hussain, A.R.J.; Alahyari, A.A.; Eastman, S.A.; Thibaud-Erkey, C.; Johnston, S.; Sobkowicz, M. Review of polymers for heat exchanger applications: Factors concerning thermal conductivity. *Appl. Therm. Eng.* **2017**, *113*, 1118–1127. [CrossRef]
11. Zaheed, L.; Jachuck, R. Review of polymer compact heat exchangers, with special emphasis on a polymer film unit. *Appl. Therm. Eng.* **2004**, *24*, 2323–2358. [CrossRef]
12. Smith, W.F. Solar Energy Absorber. U.S. Patent 4763641, 6 November 1987.
13. Shuster, J.P.; Cesaroni, A.J. Heat Exchanger Fabricated from Polymer Compositions. U.S. Patent 4955435, 11 September 1990.
14. Rasouli, E.; Strong, A.; Narayanan, V. High efficiency microchannel polymer heat exchangers for heating and cooling applications. *ASHRAE Trans.* **2020**, *126*, 341–348.
15. Harris, C.; Despa, M.; Kelly, K. Design and fabrication of a cross flow micro heat exchanger. *J. Microelectromechanical Syst.* **2000**, *9*, 502–508. [CrossRef]
16. Rajagopal, M.C.; Chang, H.C.; Man, T.; Kuntumalla, G.; Meng, Y.; Sundar, S.; Zhao, H.; Salapaka, S.; Shao, C.; Ferreira, P.; et al. Materials-to-device design of hybrid metal-polymer heat exchanger tubes for low temperature waste heat recovery. *Int. J. Heat Mass Transf.* **2019**, *143*, 118497. [CrossRef]
17. Fugmann, H.; Schnabel, L.; Frohnapfel, B. Heat transfer and pressure drop correlations for laminar flow in an in-line and staggered array of circular cylinders. *Numer. Heat Transfer Part A Appl.* **2019**, *75*, 1–20. [CrossRef]
18. Azzouz, K.; Boisselle, P.; De Vaulx, C. Heat Exchanger and Method for Manufacturing Same. International Patent WO2017162966A1, August 1994.
19. Sahiti, N. Thermal and fluid dynamic performance of pin fin heat transfer surfaces. Ph.D. Thesis, Friedrich-Alexander Universitat, Erlangen-Nurnberg, Germany, 27 January 2006.
20. Arie, M.; Hymas, D.; Singer, F.; Shooshtari, A.; Ohadi, M. Performance Characterization of a Novel Cross-Media Composite Heat Exchanger for Air-to-Liquid Applications. In Proceedings of the InterSociety Conference on Thermal and Thermomechanical Phenomena in Electronic Systems, ITherm, Las Vegas, NV, USA, 28–31 May 2019; pp. 933–940.
21. Arie, M.; Hymas, D.; Singer, F.; Shooshtari, A.; Ohadi, M. An additively manufactured novel polymer composite heat exchanger for dry cooling applications. *Int. J. Heat Mass Transf.* **2019**, *147*, 118889. [CrossRef]
22. Hymas, M.; Arle, M.A.; Singer, F.; Shooshtari, A.H.; Ohadi, M.M. Enhanced Air-Side Heat Transfer in an Additively Manufactured Polymer Composite Heat Exchanger. In Proceedings of the 16th IEEE InterSociety Conference on Thermal and Thermomechanical Phenomena in Electronic Systems, ITherm, Orlando, FL, USA, 30 May–2 June 2017; pp. 634–638. [CrossRef]

23. Kailkhura, G.; Mandel, R.K.; Shooshtari, A.H.; Ohadi, M.M. Numerical Investigation of an Integrated Cross-Media Heat Exchanger (iCMHX) for Gas-to-Liquid Cooling Applications. In Proceedings of the 19th IEEE InterSociety Conference on Thermal and Thermomechanical Phenomena in Electronic Systems, ITherm, Orlando, FL, USA, 26–29 May 2020; pp. 501–509. [CrossRef]
24. Kailkhura, G.; Mandel, R.K.; Shooshtari, A.H.; Ohadi, M.M. Experimental Study of a Set of Integrated Cross-Media Heat Exchangers (iCMHXs) for Liquid Cooling Applications in Desktop Computers. *InterPACK* **2020**, *91*, 1–58.
25. Singer, F.; Deisenroth, D.C.; Hymas, D.M.; Ohadi, M.M. Additively manufactured copper components and composite structures for thermal management applications. In Proceedings of the 16th IEEE Intersociety Conference on Thermal and Thermomechanical Phenomena in Electronic Systems (ITherm), Orlando, FL, USA, 30 May–2 June 2017; pp. 174–183. [CrossRef]
26. Hymas, S.; Dessiatoun, S.V.; Ohadi, M.M. Metal/Polymer Composite Additive Manufacturing (mfc-am) and Composite Structures Formed by mfc-am. U.S. Patent US20200016823, 16 January 2020.
27. Nazari, M.; Karami, M.; Ashouri, M. Comparing the thermal performance of water, Ethylene Glycol, Alumina and CNT nanofluids in CPU cooling: Experimental study. *Exp. Therm. Fluid Sci.* **2014**, *57*, 371–377. [CrossRef]
28. Pastukhov, V.; Maidanik, Y.; Vershinin, C.; Korukov, M. Miniature loop heat pipes for electronics cooling. *Appl. Therm. Eng.* **2003**, *23*, 1125–1135. [CrossRef]
29. Lang, T.A.; Secic, M. *How to Report Statistics in Medicine: Annotated Guidelines for Authors, Editors, and Reviewers*; American College of Physicians: Philadelphia, PA, USA, 1997.
30. Taylor, B.N.; Kuyatt, C.E. Guidelines for evaluating and expressing the uncertainty of NIST measurement results. *NIST Tech. Notes* **1994**, *1297*, 20. [CrossRef]
31. Berbish, N.S. Heat transfer and flow behavior around four staggered elliptic cylinders in cross flow. *Heat Mass Transf.* **2010**, *47*, 287–300. [CrossRef]
32. Tala, J.S.; Bougeard, D.; Russeil, S.; Harion, J.-L. Tube pattern effect on thermalhydraulic characteristics in a two-rows finned-tube heat exchanger. *Int. J. Therm. Sci.* **2012**, *60*, 225–235. [CrossRef]
33. Hasan, A. Thermal-hydraulic performance of oval tubes in a cross-flow of air. *Heat Mass Transf.* **2005**, *41*, 724–733. [CrossRef]
34. Ibrahim, T.A.; Gomaa, A. Thermal performance criteria of elliptic tube bundle in crossflow. *Int. J. Therm. Sci.* **2009**, *48*, 2148–2158. [CrossRef]
35. Jang, J.-Y.; Yang, J.-Y. Experimental and 3-D Numerical Analysis of the Thermal-Hydraulic Characteristics of Elliptic Finned-Tube Heat Exchangers. *Heat Transf. Eng.* **1998**, *19*, 55–67. [CrossRef]
36. Chen, Y.; Fiebig, M.; Mitra, N.K. Conjugate Heat Transfer of a Finned Oval Tube Part A: Flow Patterns. *Numer. Heat Transfer Part A Appl.* **1998**, *33*, 371–385. [CrossRef]
37. Bergman, T.L.; Lavine, A.S.; Incropera, F.P.; DeWitt, D.P. *Fundamentals of Heat and Mass Transfer*; John Wiley & Sons: Hoboken, NJ, USA, 2011.
38. Rodgers, P.; Goharzadeh, A.; Ali, O.A.E.; Eveloy, V. An experimental and numerical investigation of tube bank heat exchanger thermofluids. In Proceedings of the EuroSimE 2008–International Conference on Thermal, Mechanical and Multi-Physics Simulation and Experiments in Microelectronics and Microsystems, Freiburg im Breisgau, Germany, 20–23 April 2008; pp. 1–10. [CrossRef]
39. Khan, W.A.; Culham, J.R.; Yovanovich, M.M. Convection heat transfer from tube banks in crossflow: Analytical approach. *Int. J. Heat Mass Transf.* **2006**, *49*, 4831–4838. [CrossRef]
40. Tahseen, T.A.; Ishak, M.; Rahman, M. An overview on thermal and fluid flow characteristics in a plain plate finned and un-finned tube banks heat exchanger. *Renew. Sustain. Energy Rev.* **2015**, *43*, 363–380. [CrossRef]
41. Gaddis, E.S.; Gnielinski, V. Pressure drop in cross flow across tube bundles. *Int. Chem. Eng.* **1985**, *25*, 1–15. Available online: https://www.osti.gov/biblio/6503251-pressure-drop-cross-flow-across-tube-bundles (accessed on 14 January 2020).
42. El Gharbi, N.; Kheiri, A.; El Ganaoui, M.; Blanchard, R. Numerical optimization of heat exchangers with circular and non-circular shapes. *Case Stud. Therm. Eng.* **2015**, *6*, 194–203. [CrossRef]